

# Measurement and Theoretical Interpretation of Exciton Diffusion as a Function of Intermolecular Separation for Squaraines Targeted for Bulk Heterojunction Solar Cells

Chenyu Zheng, Michael F. Mark, Tyler Wiegand, Steven A. Diaz, Jeremy Cody, Frank C. Spano, David W. McCamant, and Christopher J. Collison\*

Cite This: *J. Phys. Chem. C* 2020, 124, 4032–4043

Read Online

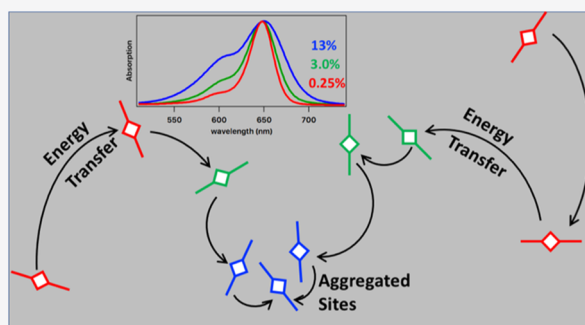
ACCESS |

Metrics & More

Article Recommendations

Supporting Information

**ABSTRACT:** The efficiency of bulk heterojunction (BHJ) organic photovoltaic (OPV) devices depends significantly upon absorption of photons and the migration of the photogenerated excited state to the heterojunction interface between the electron donor and electron acceptor. Within anilino-squaraine, molecules known for their successful use in the active layer of OPV devices, electronic aggregation strongly influences the absorption spectrum, energy transfer (EnT), and exciton migration to this heterojunction interface. Therefore, the long-range transition dipole coupling and the relative populations of the associated excited states dictate the general effectiveness of these materials in optoelectronic devices. This work presents subpicosecond transient absorption (TA) data that probe the excited-state photophysics of samples with a continuum of intermolecular separation, from monomers in solution to high-concentration solid solution thin films analogous to OPV active layers. EnT times are calculated for each squaraine concentration, and pump-power dependence provides evidence for significant EnT despite a high preponderance of H-aggregation. Theoretical modeling of essential states supports the interpretation from TA spectra that excited states relax into more tightly packed H-aggregates. This work prompts further questions regarding a far-reaching mechanistic EnT bottleneck for molecular and polymeric BHJ devices.



## INTRODUCTION

Organic photovoltaic (OPV) devices promise an excellent low-cost renewable energy solution as part of a broader portfolio of commercially viable solar cells. Their manufacture only relies upon spin-coating for prototypes with a promised transition to roll-to-roll printing or spray-coating technology for scale up.<sup>1–3</sup> Other benefits include their flexibility, allowing application to curved structures, and tunable wavelength response through chemical design. However, despite very promising dollar-per-watt projections based on the expected low-cost manufacture, organic solar cells have suffered from lower efficiencies ultimately preventing their widespread use. There have been some recent power conversion efficiency (PCE) gains<sup>4–9</sup> with low-band gap polymers and emerging non-fullerene acceptors, but a substantial need remains for new low-band gap molecular chromophores. Molecular chromophores provide advantages because sample morphology, performance reproducibility, and commercial scale-up are not complicated by the molecular weight distribution control necessary for polymer synthesis.

The challenge is that any new material must combine good transport and optical properties with consistent processing and environmental stability, in order for the commercial viability of OPVs to become a reality. High efficiencies can be recognized when the properties of the active layer materials<sup>10</sup> are tailored

toward all parts of the OPV mechanism. For example, intrinsic properties for successful active layer materials must include (i) high extinction coefficients to maximize solar photon absorption, (ii) high EnT rates for efficient exciton diffusion to a bulk heterojunction (BHJ) interface, (iii) fast electron transfer and charge separation to a coupled electron acceptor, and (iv) high carrier mobility for charge transport to an electrode. The packing of the molecules in the device influences all of these steps and each feature<sup>11,12</sup> may become a critical bottleneck reducing current generation and/or sufficient electromotive force to drive the external load.

We focus here on how exciton diffusion and EnT depend on the molecular packing of active layer materials. A bound electron–hole pair or exciton, formed by absorption of a photon, must first migrate to the BHJ interface within its lifetime. Only those excitons that can diffuse to a BHJ interface before recombining to the ground state can contribute to charge separation and photocurrent. The average distance

Received: December 21, 2019

Revised: January 1, 2020

Published: February 10, 2020

traveled by the exciton before its recombination is the exciton diffusion length. In general, isotropic fullerene acceptors are being replaced by more planar conjugated acceptors in OPV devices, and phase separation between the donor and acceptor materials is becoming more common.<sup>13</sup> Phase separation leads to larger domains that can be substantially larger than the exciton diffusion length such that fewer excitons can reach the BHJ interface for charge dissociation. Ordered molecular packing of the active layer materials is considered vital for increased charge mobility but, intuitively, tighter packing also opens channels for exciton diffusion and therefore larger exciton diffusion lengths, through Dexter-based EnT involving molecular orbital overlap.<sup>14</sup> However, short-range interaction of all conjugated molecules and polymers radically changes the photophysics in a way that the exciton diffusion may be restricted. Several review articles independently explore the importance of exciton diffusion for OPV<sup>11,15</sup> and the photophysics of aggregates,<sup>16–18</sup> but in this work, we connect the photophysics of H-aggregation of quadrupolar push–pull donor molecules and the exciton diffusion that is vital for photocurrent generation.

The packing of dye molecules into a crystal lattice allows for the formation of transition-dipole-coupled  $\pi$ -stacked aggregates or H-aggregates.<sup>18</sup> However, after initial excitation and relaxation to the lowest energy excited state, Förster EnT may be forbidden in H-aggregates because fluorescence from the lowest energy state is quantum mechanically forbidden and Förster transfer relies on the overlap integral between the donor fluorescence and the energy acceptor's absorption spectrum.<sup>19</sup> In this work, therefore, we explore exciton diffusion and EnT in squaraines (SQs) that have been successfully used as the electron donor material in solution-processed OPV but which have also been shown to form H-aggregates.<sup>20–22</sup> Incongruously, these dyes remain widely and successfully used in efficient solar cells despite EnT in H-aggregated SQs being quantum mechanically forbidden.<sup>21,23–26</sup>

SQ dyes are donor–acceptor–donor (D–A–D) molecules that are relatively easy to synthesize and purify and have high extinction coefficients in the visible and near-infrared region<sup>27–31</sup> (Note that here, the “D–A–D” structure refers to the internal molecular structure of the dye; in an OPV device, the molecule as a whole acts as the “donor” of an electron to the electron-conducting layer). A recently synthesized simple anilinic SQ, DBSQ(OH)<sub>2</sub>, has achieved a PCE of over 4.8% in solar cells in our group<sup>24</sup> but power conversion efficiencies of over 7% have been achieved for other large  $\pi$ -extended conjugated SQ devices<sup>32</sup> and over 10% for quaternary cocrystalline SQ solar cells.<sup>33</sup> The simple and high-yield synthesis, high efficiency, and strong stability of SQ materials mark the potential of this material for commercialization of OPV.<sup>26</sup> SQs are also simple enough molecules such that they can be explored theoretically and computationally as representatives of all push–pull materials.<sup>34</sup> Intermolecular charge transfer (ICT) coupling in their aggregates,<sup>23,24</sup> along with dipole and quadrupole coupling<sup>27</sup> can be investigated, and the importance of these couplings can be also applied to the design of more elaborate push–pull molecules targeted for more efficient OPV.

Our recent work shows how short-range ICT coupling and long-range Coulombic coupling are influenced by sample morphology and phase separation, driven by chemical compatibility between SQ and fullerene and control of crystallinity in thin films either upon spin-casting or after

subsequent annealing treatment.<sup>35</sup> As stated above, increased exciton diffusion rates and charge mobility, and thus improved PCE, are expected to result from highly crystalline SQ films.<sup>36,37</sup> However, our work also expressed the need to maintain small domain sizes<sup>21,24</sup> when exciton diffusion lengths are intrinsically small, and we also recognize in our data that some degree of aggregate disruption may actually lead to an increase in overall PCE. This sharply calls into question the importance of aggregates in OPV devices. On the one hand, aggregation leads to a very broad absorption profile which maximizes the overlap with the solar spectrum. On the other hand, the broad spectrum is related to an ICT state coupled to an H-aggregate and as discussed above, H-aggregation may impede diffusion by limiting Förster EnT.

We can make a comparison with work done on rhodamine 6G where dimers relax back to the ground state on a picosecond timescale.<sup>38</sup> This significant loss of fluorescence quantum yield is known as concentration quenching. Conjugated polymers have been widely used in OPV and in organic light-emitting diodes in part because they emit in the solid state and are less susceptible to this concentration quenching.<sup>39</sup> Nevertheless, SQs have been shown to work well in OPV devices and therefore any diffusion of the excited state to the BHJ interface must compete with the nonradiative relaxation of quenching centers in SQs. We consider the quenching centers to be H-aggregates and also H-aggregates coupled to ICT states.<sup>20</sup> We consider first, in this work, the impact of varying concentrations on the excited-state properties of the SQs in solid solutions, where the aggregation has been sufficiently disrupted, analogous to the structure that may be typical in the optimized as-cast SQ–fullerene OPV devices.<sup>23</sup> We investigate the excited states of both isolated SQ molecules and Coulombically coupled SQ molecules within a solid solution. To clarify, we refer to “Coulombically coupled” molecules as those molecules that are sufficiently close to one another and at an appropriate orientation that Coulombic coupling between their  $S_0$ – $S_1$  transition dipoles will lead to measurable changes in their absorption spectra. We also choose the term “Coulombically coupled” to exclude dimers that are tightly packed in a specific crystal geometry, typically <0.4 nm, for which there is additional mixing between H-aggregates and ICT states, as described by Hestand et al.<sup>20</sup> and Zheng et al.<sup>21</sup> We consider the roles of concentration quenching<sup>38</sup> and specifically of H-aggregation in EnT in OPV devices, recognizing that exciton diffusion is expected to depend on the radiative rate constant of the excited state.<sup>19</sup> We measure excited-state signatures and infer changes to the excited-state populations. We consider how EnT and exciton diffusion of these excited states are specifically impacted by an ever decreasing intermolecular separation distance. Hence, these measurements will lead to refinements in the rational design of materials for OPV to account for the limitations of aggregation quenching.

## ■ EXPERIMENTAL SECTION

**Materials.** The SQ molecule DBSQ(OH)<sub>2</sub>, (2,4-bis[4-(*N,N*-dibutylamino)-2,6-dihydroxyphenyl]squaraine) as shown in Figure 1, was synthesized according to a one-pot two-step procedure.<sup>40</sup> The corresponding amine was purchased and condensed at reflux with 1,3,5-trihydroxybenzene in a toluene/*n*-butanol (3:1, v/v) mixed solution. The yielded aniline intermediates were directly mixed with half equivalent

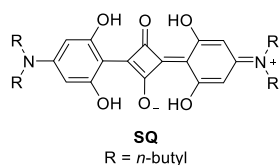


**Figure 1.** SQ molecule DBSQ(OH)<sub>2</sub>, 2,4-bis[4-(*N,N*-dibutylamino)-2,6-dihydroxyphenyl]squaraine.

squaric acid for the second condensation. The final product was a green solid and was stored in a N<sub>2</sub>-filled glovebox.

For solutions, SQ was dissolved in chloroform after weighing solids, sonicating, and heating on a hot plate at 55 °C for 5 min to ensure that the materials were fully dissolved. For polymethylmethacrylate (PMMA) polymer solid solutions (films), PMMA and SQs are codissolved in chloroform solution, with similar sonicating and heating, before being spin-cast into thin films on glass slides. The errors for the weight percent are estimated to be less than 5%. The optical densities of the films were managed to be 0.4–0.8 (except for the most-diluted sample with an optical density of ~0.1) to ensure a sufficient signal in transient absorption (TA) spectroscopy.

**Time-Correlated Single-Photon Counting.** The 800 nm output of a modelocked Newport Ti:Sapphire laser with a repetition rate of 76 MHz was sent to an optical parametric oscillator. The 1200 nm output was passed through a frequency doubling crystal and converted to the excitation wavelength of 600 nm. The beam was then split into two; one beam triggered the fast trigger diode and initiated the PicoHarp 300 picosecond timer (resolution of 4 ps) and the other beam excited the sample. The fluorescence of the sample was collected from a 1 cm cuvette at a right-angle geometry. The fluorescence photons were selected using a monochromator and detected using an avalanche photodiode. Each decay was collected until the maximum binned counts reached 10,000.

**Femtosecond TA.** A regeneratively amplified titanium:sapphire laser (Spectra-Physics Spitfire) was used to produce femtosecond laser pulses at a 1 kHz repetition rate. A home-built noncollinear parametric amplifier produced the pump pulses which were centered at 640 nm with a bandwidth of 30 nm.<sup>41,42</sup> The probe beam was created by focusing the fundamental 800 nm beam through a sapphire crystal to produce a white light continuum spanning 450–1000 nm. A mechanical chopper was used to block every other pump pulse. After the sample, the probe was dispersed by a grating spectrograph (Acton, 300 mm fl, 150 gr/mm) before reaching the CCD camera (Princeton Instruments, PIXIS 100BR). The white light spectrum was filtered using a dye solution (NIR800A, QCR Solutions Corp) to block residual 800 nm light from entering the spectrograph during sample collection. The pump/probe cross-correlation was measured via the optical Kerr effect in a 1 mm glass slide<sup>43</sup> giving an instrument response of 100 fs. For PMMA films, a spot size of 7.05 × 10<sup>-4</sup> cm<sup>2</sup> was used to minimize the potential effects of singlet–singlet annihilation. For the most dilute PMMA sample (0.01%) and for the dye in chloroform (CHCl<sub>3</sub>), the pump beam was focused more tightly to increase the signal intensity compared to that for the aggregated PMMA samples. TA data were collected at three powers of 20, 40, and 80 nJ/pulse. To prevent photobleaching, the thin films were translated rapidly in both the *x* and *y* directions via automated stages. TA data of

samples in CHCl<sub>3</sub> were collected in a 2 mm fused silica cuvette with a total absorbance of 0.7. The sample was translated vertically during the experiment to continuously refresh the sampling spot.

The TA signal was collected at parallel and perpendicular pump polarizations relative to the probe, to obtain the isotropic signal

$$\Delta A_{\text{Iso}} = \frac{(\Delta A_{\parallel} + 2\Delta A_{\perp})}{3} \quad (1)$$

Transient anisotropy traces were calculated via

$$\rho(t) = \frac{(\Delta A_{\parallel} - \Delta A_{\perp})}{(\Delta A_{\parallel} + 2\Delta A_{\perp})} \quad (2)$$

## EXPERIMENTAL RESULTS AND DISCUSSION

**Steady-State Absorption.** The normalized absorption spectra of SQ in CHCl<sub>3</sub> and PMMA films are presented in Figure 2. As depicted, the absorption in CHCl<sub>3</sub> (black, dashed)

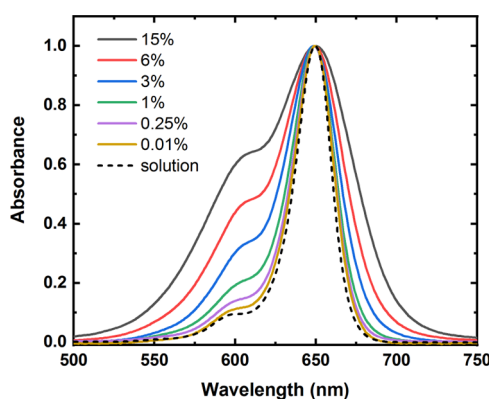


**Figure 2.** Normalized absorption spectra of SQ in chloroform solution and PMMA solid solutions at different weight ratios.

is typical of monomeric SQs in solution,<sup>20,24</sup> with a  $\lambda_{\text{max}}$  at 649 nm representing the  $S_0(v=0) \rightarrow S_1(v=0)$  band, referred to as “0–0”. A low intensity Franck–Condon shoulder indicates the  $S_0(v=0) \rightarrow S_1(v=1)$  or the “0–1” transition appearing at 597 nm. When SQ/PMMA solid solutions are spin-cast, the absorption profile is shown to broaden and the 0–1 vibronic transition gains intensity as the wt % of SQ increases from 0.01 to 15%. The relative increase of the 0–1 vibronic transition compared to that of the 0–0 transition typically indicates the formation of H-aggregates having face-to-face transition dipole moment (TDM) arrangements.<sup>18,44</sup> As the SQ weight ratio increases, the average distance between chromophores in the PMMA solid solution decreases, resulting in stronger intermolecular interactions and subsequently higher intensity 0–1 peaks.<sup>23</sup> These data will be explored further below.

**Theoretical Modeling of SQ Absorption Spectra.** The CHCl<sub>3</sub> solution spectrum of DBSQ(OH)<sub>2</sub>, as represented in Figure 2, has been described well using an essential states model (ESM) pioneered by Painelli.<sup>55,56</sup> The ESM has been particularly successful at rationalizing spectral behaviors in such push–pull type chromophores and their aggregates.<sup>55</sup> Hestand et al. and Zheng et al. have expanded the model, applying it to SQs, to describe how spectral features in neat films result from Coulombic (transition dipole) coupling of H-aggregation and an ICT interaction.<sup>20,21</sup> However, in the



current system, it is unclear if the spectra are due to the existence of both monomeric and aggregated species in the films, as would be expected if the SQ began to precipitate out during spin-casting, or if the chromophores can be treated as having a continuous distribution of distances, which would occur if the dyes were trapped in a solution-like distribution by rapid solvent evaporation during casting. Hence, we will test the simpler solution-like distribution model to assess whether it can explain the shapes of the absorption spectra. Given the longer range interactions between neighboring SQs in these PMMA solid solutions compared to neat films, we here apply the ESM to investigate only the Coulombic interaction, that is, transition dipole coupling, while neglecting the ICT, which requires neighboring orbital overlap. It is the Coulombic interaction that is expected to describe the increasing ratio of 0–1/0–0 peaks as the SQ concentration increases.

A summary of our theoretical approach follows, with more complete explanations found elsewhere.<sup>20–22</sup> For our symmetric SQ molecules, the relevant ground and excited states are described by three diabatic states, namely,  $D^+-A^--D$  ( $|Z_1\rangle$ ),  $D-A-D$  ( $|N\rangle$ ), and  $D-A^--D^+$  ( $|Z_2\rangle$ ), corresponding to each of three resonance structures for a greatly simplified molecule of two peripheral nitrogens each connected to a central squarylium through a conjugated bridge. Each zwitterionic state,  $Z_1$  and  $Z_2$ , possesses an energy of  $\eta$  over the neutral state,  $N$ , and can couple to the neutral state with a charge transfer integral  $t$ . Molecular vibrations are accounted for by introducing vibrational quanta to the simplified conjugated bridge for each molecular arm. The electron–phonon coupling is considered by shifting the vibrational coordinate for the arm that holds a zwitterion. Thus, the complete monomer Hamiltonian reads

$$\hat{H}_{\text{mon}} = \eta \sum_{a=1}^2 |Z_a\rangle \langle Z_a| - t \sum_{a=1}^2 \{|N\rangle \langle Z_a|\} + \text{h. c.} \\ + \omega_0 \sum_{a=1}^2 b_a^\dagger b_a + \omega_0 \lambda \sum_{a=1}^2 (b_a^\dagger + b_a + \lambda) |Z_a\rangle \langle Z_a| \quad (3)$$

with  $b_a^\dagger$  ( $b_a$ ) the creation (annihilation) operator for vibrational quanta on the harmonic oscillators corresponding to the neutral and zwitterionic arms [ $a = 1$  (2) for the left (right) arm]. Here, the vibrational levels are assumed to be equally spaced by an energy of  $\omega_0$  (noting that  $\hbar$  is taken to be 1).  $\lambda$  describes the displacement of the nuclear equilibrium positions of the zwitterionic and neutral arm ( $\lambda^2$  is the *adiabatic* Huang–Rhys parameter). The monomer Hamiltonian of eq 3 was parameterized by best fitting simulations to the SQ monomer absorption spectrum in chloroform (see Figure 2a). The following fit parameters are consistent with reported results:<sup>20</sup>  $\eta = 0.69$  eV,  $t = -1.05$  eV,  $\omega_0 = 0.16$  eV, and  $\lambda^2 = 1$ . The simulated monomer absorption spectrum is shown in Figure 3 along with the experimental spectrum obtained from the chloroform solution, demonstrating good agreement between the theory and the experiment.

The Hamiltonian for a concentrated solution must properly account for the intermolecular interactions in addition to the monomer diabatic states. The Coulombic coupling between chromophores in the aggregates is considered in the diabatic basis by placing point charges on the center of the squarylium and the two nitrogen atoms (relevant to  $|Z_1\rangle$  or  $|Z_2\rangle$  state). Thus, the aggregate Hamiltonian is written as

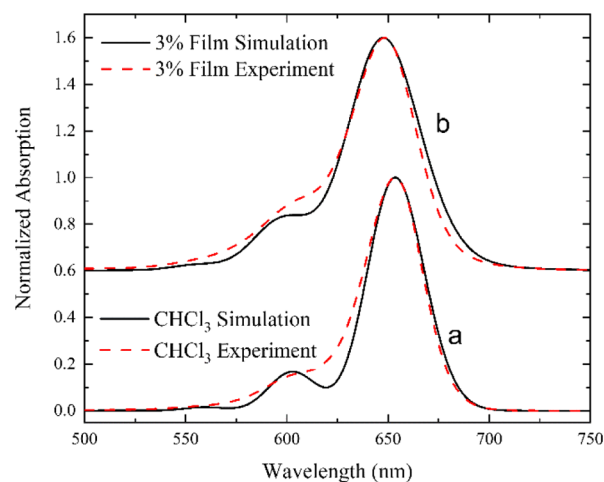


**Figure 3.** Simulation of (a) monomer absorption spectra using eq 4 and (b) dimer absorption spectra using eq 4 plotted against the measured 3% SQ in PMMA steady-state absorption spectrum. The simulated spectra have all been shifted to shorter wavelengths by 0.086 eV (30.7 nm at 650 nm) for comparison with experiment.

$$\hat{H}_{\text{agg}} = \sum_{n=1} \hat{H}_n^{\text{mon}} + \hat{V} \quad (4)$$

where  $n$  represents the number of molecules in the aggregate and  $\hat{V}$  is the Coulomb term.<sup>22</sup> Diagonalizing the Hamiltonian in eq 4 transforms  $\hat{V}$  into a term that acts to split the excited state, analogous to Kasha's molecular exciton theory<sup>49</sup> but with some key differences. Full details of these differences and of the calculations of the TDM and oscillator strength for optical absorption are found in our prior work.<sup>22</sup> Importantly, we consider a dimer ( $n = 2$ ) as an effective model for the Coulombically coupled SQ aggregate species in PMMA solid solution films. Extending the Hamiltonian in eq 4 to SQ dimers, all the fit parameters from the monomer are used, but the Coulombic interaction terms are dependent on the molecular geometry.

In a single crystal structure of DBSQ(OH)<sub>2</sub>,<sup>24</sup> the molecules are packed in a specific slip-stacked manner with one molecule per unit cell. However, in our randomized solid solution, we consider all relative orientation angles, weighted geometrically after taking into account the probabilities of nearest neighbors for each concentration studied. The mathematical form of the interaction of two dipoles in space is well-understood.<sup>14,18,19</sup> In general, the strength of the dipole–dipole interaction depends on the magnitudes of the individual dipoles, the distance separating the centers of the two dipoles, and the orientation angle of the dipoles relative to each other.<sup>53</sup>

The Coulombic interactions of neighboring molecules that are well-separated are different (and will yield different results) from our previous work where the exact single crystal geometry, together with ICT considerations, led to a unique “double hump” absorption profile in neat films.<sup>20</sup> When dispersed in PMMA solid solutions, we consider the interplanar distance  $R$  (Figure 4) to be much larger than that in the single crystal. Therefore, the ICT is not likely to take place as it depends on molecular orbital overlap and is consequently very sensitive to the intermolecular separation. Furthermore, the absorption spectra in PMMA films show no sign of ICT-induced splitting of electronic peaks.

In order to account for our randomized solid solution PMMA samples, there are three parts to the simulation. First,

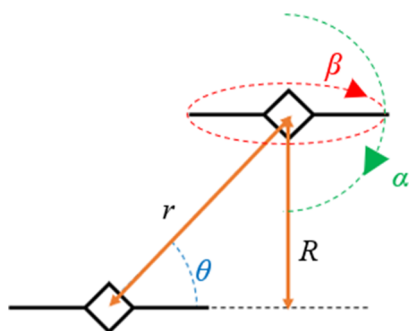


**Figure 4.** Visualization of the parameters considered when identifying relative positions of nearest-neighbor chromophores.

the individual spectrum for each unique orientation angle between molecules was established as a function of distance  $r$  and angles  $\theta$ ,  $\alpha$ , and  $\beta$  (The geometry of interaction for two randomized nearest neighbors is presented in Figure 4). Second, the spectrum was weighted to recognize the changing circumference of the circle with the changing radius  $R$  and was appropriately weighted for each set of angles  $\alpha$  and  $\beta$ . Third, the (nearest neighbor) distribution of intermolecular separation distances was accommodated by summing the calculated spectra for each separation distance  $r$ , weighted appropriately for the probability of that distance, given the overall concentration (Figures S6 and S7).

The simulation spectra presented in Figures 3 and 5 thus include weighted sums of all simulated spectra for each set of

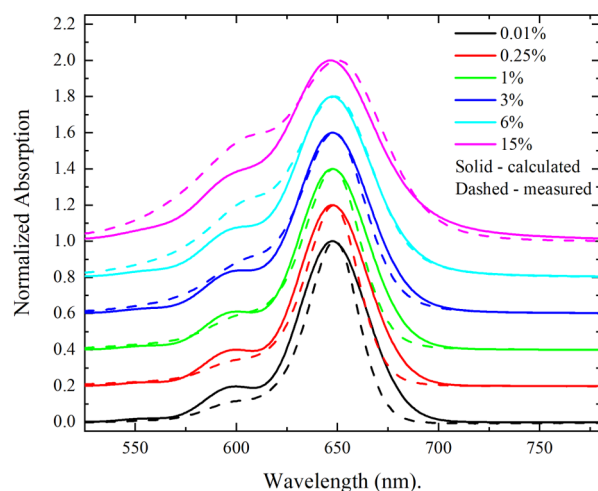


**Figure 5.** Simulation of dimer absorption spectra for all samples accounting for a complete nearest-neighbor distance distribution and weighting for all possible orientation angles between a central molecule and a surrounding molecule (see text and Figure S7).

individual orientations and distances. For example, the experimental spectrum for the 3% SQ film and the simulation over all orientations and the corresponding nearest-neighbor spatial distribution is shown in Figure 3 (upper spectra). The simulations consistently produce spectra whose spectrum is at lower energy than the experiment, but for clarity, they have been blue-shifted by 0.086 eV to align the 0–0 peaks and facilitate the comparison of the overall shapes, as shown in Figure 5. As the SQ concentration increases, the simulated data faithfully follow the observed increase in the ratio of 0–1 transition to 0–0 transition, although the rate of increase of

this ratio is lower in the simulation. For each simulation, the same broadening factor was applied to each calculated transition. The correlation between the simulated spectra and measured data strongly supports the validity of the theoretical approach and agrees with the work of Zheng et al.<sup>22</sup> The ability of the simulation to reproduce the major components of the absorption spectra indicates that there is no significant presence of a fully aggregated population, in which the chromophores take on a pi-stacked arrangement as in the crystal structure or an annealed OPV film.<sup>21</sup> Rather, we are able to reproduce the major characteristics of the spectra by treating the sample as a solid solution, in which the distribution of nearest-neighbor distances varies continuously from close-packed to distant with a near-Gaussian probability and the orientation of the chromophores is entirely random.

In the experimental data from Figure 5a, there is no convincing evidence of any J-aggregate coupling, even though a random distribution of closely spaced dipoles would show such a signature. However, as described by Zheng et al.,<sup>22</sup> these data are consistent with a divergence from conventional (Kasha) J-aggregate behavior when quadrupolar interactions exist over short intermolecular separation distances. Zheng et al. also describe how the quadrupolar interactions will lead to increasing high energy H-aggregate dark states and red-shifted H-aggregates with dark low-energy states, for a randomized orientation geometry, as the intermolecular separation is reduced.

In addition to a simulation of the measured steady-state spectra that sums over all orientations and distances, we have independently simulated spectra accounting for all angles ( $\theta$ ,  $\alpha$ ,  $\beta$ ), but each spectrum is associated with a fixed distance  $r$  between the central molecule and the neighbor (Figure 6). In

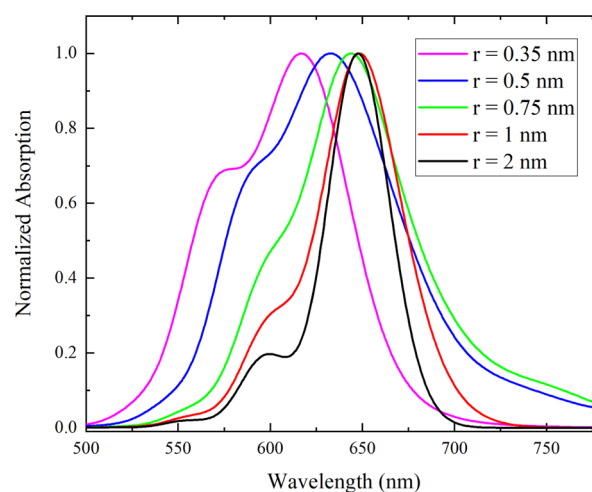


**Figure 6.** Simulation of dimer absorption spectra (using eq 4) accounting for angles of orientation ( $\theta$ ,  $\alpha$ ,  $\beta$ ) but for fixed distances  $r$  (0.35–2.0 nm). The simulated spectra have all been shifted to shorter wavelengths by 0.086 eV (30.7 nm at 650 nm) for comparison with experimental data.

order to clearly see the effect of the decreasing distance between dimers, we have removed the weighting for the distribution of separation distances which is predicted from the nearest-neighbor model. As expected, we observe a steady blue shift to shorter wavelengths along with an increased ratio of 0–1/0–0 bands as the intermolecular separation distance  $r$  decreases below 0.5 nm. This verifies an expected means to

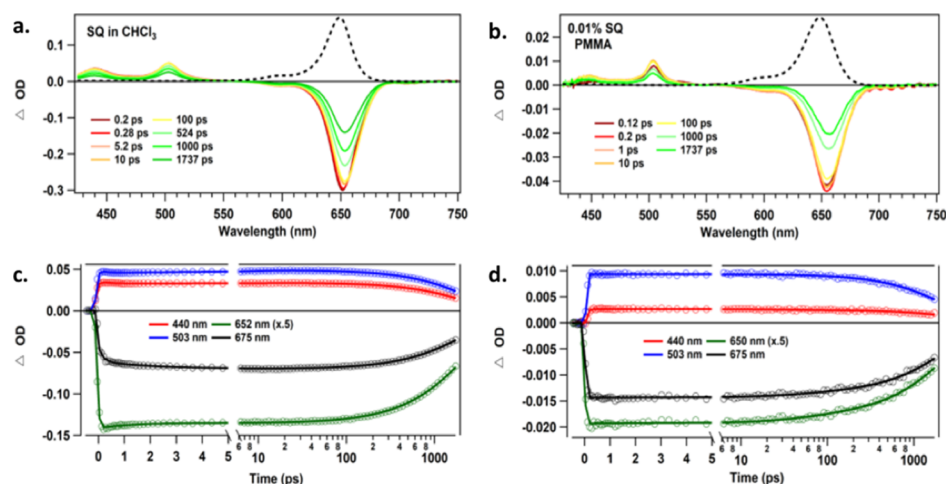


**Figure 7.** Steady-state absorption (black dotted line, a,b) and TA spectra (solid lines, a,b) and kinetic traces (c,d) for SQ in CHCl<sub>3</sub> (left) and in dilute PMMA films (0.01 wt %, right) after excitation at 640 nm. The kinetics are presented on a linear time scale from -1 to 5 ps and on a logarithmic scale from 6 to 1700 ps.

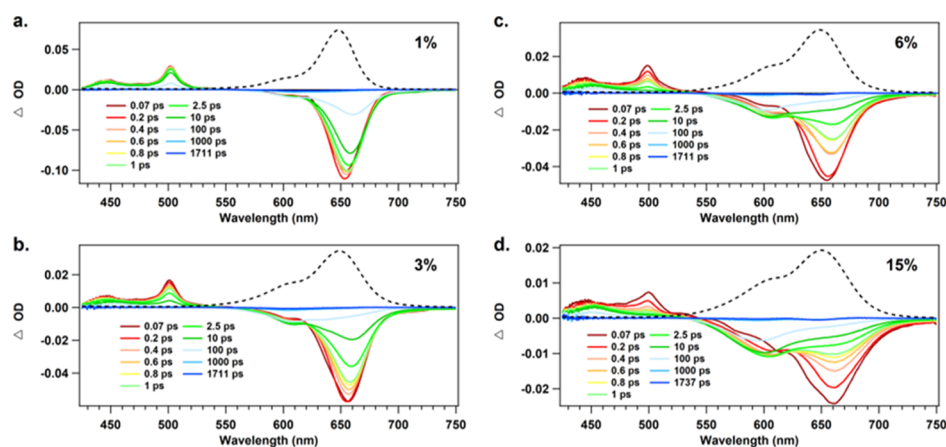


**Figure 8.** TA spectra of SQ in PMMA films with increasing wt % after excitation at 640 nm. The ground-state absorption spectrum is shown as dashed lines in each panel.

identify the environment of an exciton in the films: if excitons migrate to areas in which the chromophores are closer together, the ground-state bleach of the TA signal should blue-shift and shows an increasing amplitude in the 0–1 transition region around 600 nm.

**Transient Absorption Spectra. TA of Monomers.** TA data were collected for isolated SQ monomers, first in dilute chloroform (CHCl<sub>3</sub>) solution and then in dilute (0.01% SQ) PMMA solid solution (with a thickness of tens of micrometers). With expected large average intermolecular distances in both of these samples, the possibility of aggregation is ruled out and by comparing them, we can determine any effects of the PMMA matrix in our analysis.

The TA spectra of monomeric SQ are presented in the top panels of Figure 7 in neat CHCl<sub>3</sub> (left) and 0.01 wt % in PMMA (right). A ground-state bleach (GSB, negative signal) is present in all these spectra at ~650 nm, which mirrors the corresponding absorption spectrum (shown as a black dotted line in Figure 7a,b), while the excited-state absorption (ESA, positive signal) appears with two bands at 440 and 503 nm. In CHCl<sub>3</sub> solution, the dynamics are dominated by a 2400 ps exponential decay, observed in both the recovery of the GSB and the decay of the ESA signals. There are very minor shifts in the spectra occurring with time constants of 200 fs, 1.63 ps,

and 11.9 ps, which we assign to fast solvent and internal reorganization. This assignment is supported by the growth of stimulated emission (SE) at 675 nm on the 0.2–10 ps time scale (Figure 7c) because of the dynamic Stokes shift. The SE assignment is based on the measured fluorescence spectrum, which overlaps the absorption spectrum significantly, as is typical and expected for all SQ dilute solution samples.<sup>45</sup> Time-correlated single-photon counting measurements, as shown in Figure S1, found a fluorescence decay time of 2300 ps, slightly shorter than what was obtained from the TA fits. However, we consider these to be in good agreement, given the distribution of time constants in the wavelength-dependent TA traces (Table S2). **Transient anisotropy measurements (Figure S2) yielded a rotational correlation time of 220 ps, agreeing with prior measurements of similar SQs in solutions.**<sup>46</sup>

For the 0.01% SQ PMMA solid solution, the TA kinetics can also be fit with a decay time constant of 2400 ps that measures the excited-state lifetime (Figure 7d). Unlike when dissolved in CHCl<sub>3</sub>, 0.01% SQ does not show the same early time dynamics associated with solvent reorganization but only a slow decay in the signal as it relaxes from the excited state. Likely, the fixed structure of SQ in the rigid PMMA matrix hinders any structural rearrangement, preventing spectral shifts



on short time scales. Nevertheless, the total lifetimes observed in both 0.01% SQ PMMA and  $\text{CHCl}_3$  are similar, confirming that PMMA is a noninteracting medium and that in the 0.01% sample, molecules are sufficiently far apart to prevent any intermolecular interaction that would consequently decrease the lifetime (vide infra).

**TA of Concentrated SQ Samples in PMMA.** The TA spectra of SQ in 1–15 wt % PMMA films are presented in Figure 8. Upon photoexcitation, all samples show an instantaneous GSB at 650–660 nm, mirroring the ground-state absorption, along with an ESA having positive amplitude peaks at 440 and 500 nm like those observed for monomeric SQ. For the low concentration sample, 1% SQ (Figure 8a), the initial spectrum appears to be nearly identical to those of SQ in  $\text{CHCl}_3$  and 0.01% SQ in both breadth and wavelength. However, as the spectrum evolves, a clear Stokes shift of the SE is observed and  $\sim 75\%$  of these monomer features decay in the first 1 ns, significantly faster than for the 0.01% or solution samples.

Concurrent with the early loss of the signal at the 0–0 wavelength for each sample, a growth of the negative signal is observed near 600 nm, overlapping with the high-energy 0–1 vibronic band. The  $\lambda_{\text{max}}$  of the GSB band near 600 nm continues to slightly blue-shift at higher wt %, indicating that the bleach may be due to the population of dimers that are closely packed enough to have strong transition dipole coupling resulting in the characteristic H-aggregate absorption spectrum.<sup>44</sup> We hypothesize that the higher wt % samples contain more tightly coupled chromophores resulting in the blue-shifting GSB.<sup>23</sup> The relative magnitude (amplitude) of the growth of the negative signal at  $\sim 600$  nm is larger in the higher concentration SQ samples and seems to correspond to more effective EnT from the monomer population to aggregate populations. Assuming that the blue shift is associated with tighter Coulombic transition dipole interaction, we also observe more redistribution of the GSB signal to aggregates as concentration increases.

In Figure 9a, we compare the TA signals of each sample at 100 ps, when, at 3% SQ or higher, all monomeric features have decayed. Hence, for the  $>3\%$  SQ samples, these signals correspond to the GSB and ESA of the strongly coupled species formed both by initial excitation and by EnT from the monomer-like population. The blue shift of the GSB to shorter wavelengths with increasing SQ concentration is clearly visible. In Figure 9a, the spectrum for 1% SQ (black) at 100 ps retains ESA at 500 and GSB at 660 nm, corresponding with the monomer-excited state. Only a small shoulder near 600 nm is observed in the bleach, resulting from only a minor enhancement of the 0–1 band associated with H-aggregate formation. As concentration increases to 3% SQ (Figure 9a, green), an increase of the 0–1/0–0 band ratio is observed and a broad bleach remains, extending to  $\sim 720$  nm. The lack of the sharp ESA at 500 nm indicates that no excited monomer population is present at 100 ps in these samples and hence, the negative signals at wavelengths  $>650$  nm will contain negligible monomer SE. At the highest concentrations of 6% SQ (blue) and 15% SQ (red), the dominance of the 0–1 absorption band in the GSB indicates that the excited species are dominated by aggregated, coupled chromophores at 100 ps and that the initially excited monomer-like species have decayed, consistent with the simulated spectra as shown in Figure 6 above. At the same time, we note that there is no convincing evidence (with only minor broadening out to 720 nm)<sup>23</sup> of the J-aggregate

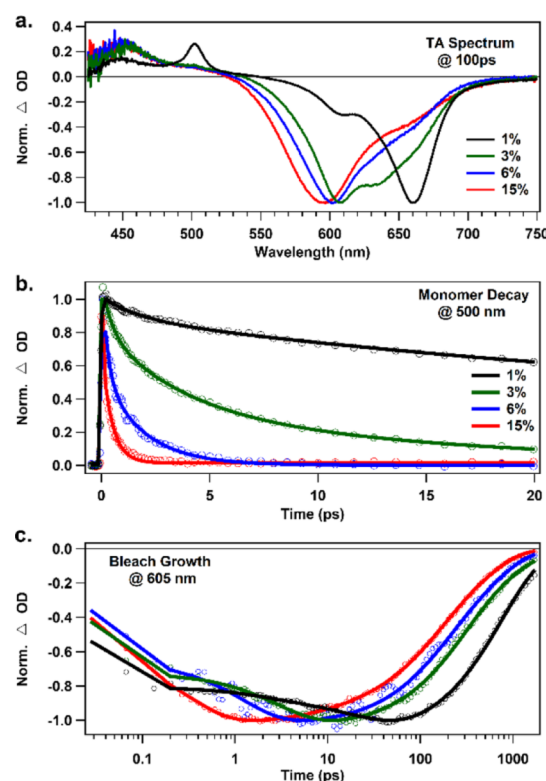


**Figure 9.** (a) TA spectra for each wt % sample at 100 ps. (b) Normalized decay kinetics at 500 nm for each aggregated PMMA sample. (c) Normalized kinetics at 600 nm plotted on a logarithmic x-axis showing an aggregate population increase resulting from EnT. Kinetic traces in (b) have been background-corrected so as to isolate only the intensity of the sharp feature at 500 nm.

coupling that one might expect for such a random distribution of molecule–molecule geometric alignments. We also note that spectral shape of the aggregate bleach in the 3, 6, and 15% samples, as shown in Figure 5a, is not static at all time delays. In Figure S5, we show that the position of the bleach dynamically shifts to shorter wavelengths as a function of time, indicating that the exciton population is moving within the distribution of SQs to species that are closer to each other and therefore have stronger coupling.

Average lifetimes for the aggregates were defined as the amplitude weighted average time constant for each sample's decay at the  $\lambda_{\text{max}}$  of the aggregate bleach ( $\sim 600$  nm). Average lifetimes are presented in Table 1 and were found to decrease with the increasing concentration. The shortest lifetime of 250 ps was found for 15% SQ, whereas the 1% SQ sample showed an average lifetime of 663 ps.

Given that the loss of the monomer signal at 500 nm and 650–660 nm coincides with growth in the aggregate bleach at 600 nm and that isosbestic points at ca. 620 nm are observed, as shown in Figure 8, during these initial events, we assign the initial events to EnT from the monomer-like species to more Coulombically coupled species. The dynamics of this EnT are shown in Figure 9 in both the decay of the monomeric ESA at 500 nm (Figure 9b) and the growth of the aggregate GSB at 600 nm (Figure 9c). Figure 9b depicts the normalized loss of the signal at 500 nm for each %wt sample. Because there are overlapping signals, the kinetics of the isolated “monomer” ESA peak were extracted from the total TA signal after subtracting the background signal on either side of the peak.

**Table 1. Average Aggregate Lifetimes and EnT Times of SQ in PMMA Films at Different wt %**

		1% SQ	3% SQ	6% SQ	15% SQ
average aggregate lifetimes (600 nm)	$\tau_1$	663 ps	627 ps	323 ps	250 ps
average monomer $\rightarrow$ aggregate EnT <sup>a</sup>	$\tau_1$	3.17 ps (~25%)	0.56 ps (~30%)	1.50 ps	0.34 ps
	$\tau_2$	31 ps (~75%)	4.0 ps (~70%)		

<sup>a</sup>Values are averages from wavelength-dependent kinetic traces. Only values of  $\tau$  which exhibit a growth of amplitude at 600 nm and with a simultaneous loss at 500 nm were averaged to best represent EnT.

For 1% SQ (black) and 3% SQ (green) traces, the monomeric absorbance persists beyond the displayed 20 ps window. The 6% SQ (blue) and 15% SQ (red) samples, however, decay to zero in <5 ps, qualitatively showing how concentration has a substantial impact on the lifetime of monomers in each sample. There is a significant acceleration of the loss of the monomeric signal at 500 nm as the concentration increases; the monomer disappears in <2 ps for 15% SQ. We compare this 500 nm decay to the growth of amplitude at 605 nm as shown in Figure 9c. For 1% SQ, the aggregate bleach at 605 nm reaches a maximum near 100 ps but as the SQ concentration increases, the maximum amplitude is reached at earlier times with the most concentrated, 15% SQ, reaching its apex near 1 ps. The time constants common to 500 nm decay and 605 nm bleach growth are shown in Table 1. These have been averaged through a global fit to best represent the EnT. For 1% SQ and 3% SQ, average rates of EnT were found to be biexponential having long time constants of 31 and 4.0 ps, respectively. At higher concentrations of 6% SQ and 15% SQ, samples were found to undergo EnT following single exponential fits of 1.50 and 0.34 ps, respectively.

**EnT between Uncoupled Chromophores.** *TA Anisotropy.* TA polarization anisotropy,  $\rho(t)$ , can decay either by molecular rotation in solution or by EnT between fixed chromophores that do not have perfectly parallel transition dipoles.<sup>47</sup> In CHCl<sub>3</sub>, it was observed (Figure S2) that the anisotropy decays with a 220 ps time constant which we can assign to the rotational correlation time of SQ in liquid solution. However, when the dyes are fixed in position by the rigid PMMA matrix, the rotational correlation time is expected to be effectively infinite, so the only possible mechanism for decay of the anisotropy must be EnT. The measured transient anisotropy data are presented in Figure 10 and Table 2. Here, the excitation from the originally excited donor transfers to a nearby acceptor having a differently oriented transition moment,<sup>48,49</sup> thus creating a loss in  $\rho$  which coincides with the rate of EnT.<sup>50</sup> The results show that the anisotropy decay accelerates in the more highly concentrated samples, paralleling the acceleration of EnT seen in the fits of TA intensity. This further supports the enhanced coupling between molecules, which we consider to be responsible for the increasing EnT rates (see Figure S2).

To place the measured TA time constants in context, we can compare them against calculated average EnT rates for SQ distributed in the PMMA matrix based on a Förster resonance EnT (FRET) mechanism.<sup>19</sup> The EnT rate will depend on (i) the intermolecular separation, (ii) the radiative rate constant, and (iii) the overlap integral between emission and absorption, which is described below. The average nearest-neighbor separation distances between monomers in the solid solution

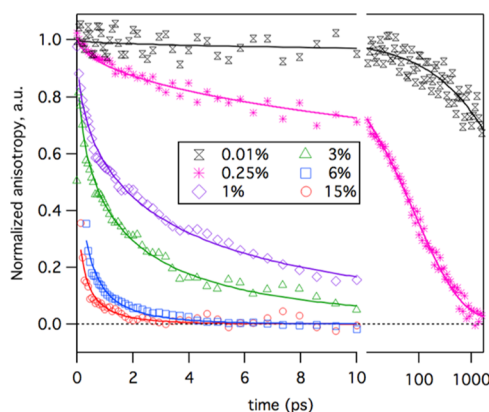


**Figure 10.** Transient anisotropy kinetics for 0.01–15 wt % SQ samples. Solid lines indicate the best-fit stretched exponential kinetics, with time constants summarized in Table 2. The time axis is linear to 10 ps and logarithmic from 10 to 1700 ps.

for the various SQ samples are shown in Table 2. This model of a dispersed solid solution is supported by the simulations of the absorption spectra (Figure 5) that indicated that the monomers are completely monodispersed in the PMMA matrix and that there is no spontaneous agglomeration of SQs during the spin-casting process or in solution before spin-casting. The probability for a nearest neighbor (of a centralized SQ) at the distance  $r$  within a shell of thickness  $dr$  can be calculated as the probability that there is no second molecule within a radial distance  $r$  multiplied by the probability that there is a second SQ molecule in the spherical shell spanning radial distance  $r$  and radial distance  $r + dr$ . A full description of the nearest-neighbor probability distribution function is presented in Figure S6 and elsewhere.<sup>51,52</sup> The concentration of the SQ (number of molecules per volume of solid solution) can be estimated from the weight percent of the SQ (% wt) and PMMA in the spin-casting solution, the molecular weight of the DBSQ(OH)<sub>2</sub> SQ (MW), Avogadro's number ( $N_A$ ), and the density ( $D$ ) of the PMMA polymer (1.18 mg/cm<sup>3</sup>).<sup>23</sup>

The SQ absorption and emission spectra in solution are used to independently estimate the Förster distance for monomer-to-monomer energy homotransfer to be  $R_0 = 7.34$  nm, allowing us to calculate the expected FRET rates for each concentration.<sup>47</sup> The results shown in Table 2 indicate that there will be little homotransfer between dyes in the 0.01% sample but that all samples above 0.25% will undergo significant EnT by homotransfer among nearest neighbors. Additionally, the distribution of nearest-neighbor distances (Figure S6) indicates that a significant percentage of dyes in the 6 and 15% samples will have nearest neighbors within 0.4 nm, a range in which strong transition dipole coupling can significantly distort the absorption spectrum of the coupled dimer.

**TA Power Dependence and Exciton–Exciton Annihilation.** Given the mobility of excited states in these samples, we further investigated the power dependence to gain some insight into the exciton diffusion that is the foundation of the efficient OPV operation. We expect a power dependence on the monomer ESA decay at 500 nm because the efficiency of EnT with the monomer population could lead to exciton–exciton annihilation as the concentration of excitons increases with increasing pump power. However, we also explored the possibility of power dependence for the aggregate GSB at 600 nm, which would indicate exciton mobility within the closely



Table 2. Concentrations, Nearest-Neighbor Distances, and Resultant Average EnT Time Constants for Different wt % Samples

wt %, SQ in PMMA	$c^a$ , nm <sup>-3</sup>	$r_{NN}^b$ , nm	$\tau_{FRET}^c$ , ps	$\tau_{FRET}^d$ calc'd ps	$\tau_{FRET}^e$ obsv'd ps
0.01%	$1.29 \times 10^{-4}$	11.0	$3.02 \times 10^4$	$5.27 \times 10^4$	$1.2(1) \times 10^4$
0.25%	0.00321	3.75	48.3	85.1	86(3)
1%	0.0129	2.36	3.02	5.27	3.1(1)
3%	0.0386	1.64	0.335	0.589	1.27(5)
6%	0.0771	1.30	0.0839	0.148	0.223(25)
15%	0.193	0.959	0.0134	0.0235	0.106(14)

<sup>a</sup>Concentration in units of molecules of SQ per cubic nanometer (nm<sup>-3</sup>). <sup>b</sup>Average nearest-neighbor distances are calculated from the concentration.<sup>51,52</sup> <sup>c</sup>The FRET time constant at the average nearest-neighbor distance is  $\tau_{FRET} = \tau_D(r/R_0)^6$ , in which  $R_0 = 7.34$  nm. However, this time constant does not predict the actual dynamics because the distribution of nearest-neighbor distances covers a huge range of FRET rates that result in stretched exponential decays. <sup>d</sup>Calculated stretched exponential time constant,  $\tau_{FRET}$ , using the Baumann–Fayer theory.<sup>50</sup> <sup>e</sup>Experimental stretched exponential  $\tau_{FRET}$  observed by fitting the TA anisotropy decays at 660 nm to the general form,  $\rho(t) = \rho_{offset} + \rho_0 \Delta \exp(-\sqrt{t/\tau_{FRET}})$ .

packed population. The time constants and amplitudes of the monomer signal at 500 nm for each wt % SQ sample, which represent the time constants for EnT ( $1/k_{EnT}$ ) to more aggregated species, at increasing powers are found in Figure S3 and Table S1. Figure 11a shows the weighted average lifetime

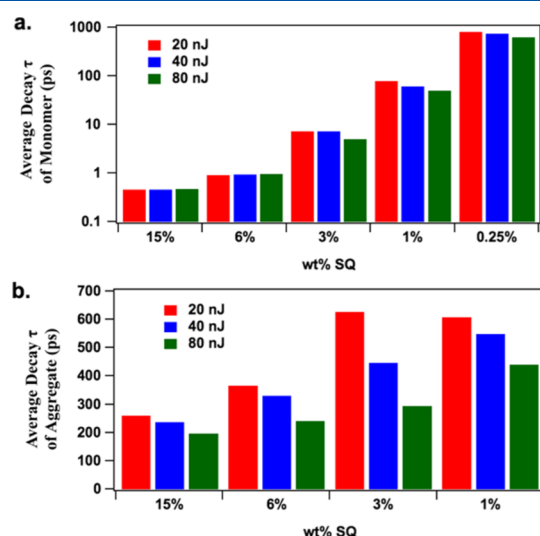


Figure 11. (a) Weighted average lifetime of the monomer-like species in PMMA films. (b) Weighted average lifetime of the aggregate-like species taken at the maximum in the aggregate bleach signal around 600 nm.

for each fit at 500 nm for powers of 20, 40, and 80 nJ/pulse. As seen, there is no change in the average monomer decay time in the highest concentration samples (15% SQ and 6% SQ), while the average decay time decreases as power is increased for the less-concentrated samples (3% SQ and 1% SQ). This lack of power dependence strongly supports our interpretation that for highly concentrated samples, there has been close to total EnT from monomers to aggregated chromophores, occurring in just 1.5 ps for 6% SQ and 0.3 ps for 15% SQ (Table 1); the faster EnT process outcompetes the relatively slower exciton–exciton annihilation within the excited-state monomer population, thereby preventing power-dependent kinetics. The power dependence of 3% SQ and 1% SQ, which exhibit faster 500 nm decays at higher powers, shows that the mobility of the exciton within these monomer populations in combination with the slower EnT to closely packed species makes annihilation competitive with EnT when the molecular separation distance is large and the presence of strongly coupled chromophores is less common. Interestingly, for

0.25% SQ, there is a decrease in lifetime of  $\sim 25\%$  between powers of 20 and 80 nJ/pulse. In this case, the absorption spectrum shows no presence of aggregates nor is there a growth of the aggregate GSB at 600 nm (Figure S4). The occurrence of annihilation and the coincidence between the observed lifetimes and the expected monomer FRET time constants (Table 2) suggest that because there are few aggregates in this sample, exciton–exciton annihilation occurs by EnT between monomers (homotransfer) that are on average  $\sim 3.7$  nm apart (Table 2).

The effect of the pump power and hence exciton–exciton annihilation on the average lifetime of the *closely packed* species observed at 600 nm is found in Figure 11b. The lifetimes of the aggregates are significantly longer than the monomer populations for samples with wt % > 0.25% and the lifetimes are concentration-dependent. In each case, we observe a substantial power dependence in which the higher pulse energies induce a large decrease in the lifetime of the *aggregate* GSB signal. This indicates that excitons in the closely packed population are still mobile such that a higher density of excitons will lead to an increased annihilation rate. This contrasts with the picture of the H-aggregated species as compromised-fluorescence trap states for excitons. Unfortunately, the aggregate–aggregate transfer rate cannot be extracted easily from the more complex pump power dependence data, despite a clear loss of aggregate excitons due to singlet–singlet annihilation.

In summary, the TA data support the following conclusions: (i) the decay of the anisotropy accelerates with increasing concentration, indicating that exciton hopping accelerates from an average time scale of 3 ps for 1% SQ to 0.1 ps for 15% SQ. (ii) EnT induces migration of excitons from weakly coupled sites to strongly coupled dimers resembling H-aggregates in  $\sim 32$  ps for 1% SQ and  $\sim 0.34$  ps for 15% SQ. (iii) Within aggregated sites, they continue to migrate toward ever more Coulombically coupled sites, as evidenced by the continuous shifting of the 0–1 absorption band at 595–610 nm to shorter wavelengths at longer delays. (iv) The lifetime of excitons in the aggregated sites decreases as the concentration increases, going from 663 ps for 1% SQ to 250 ps for 15% SQ, indicating that excitons in aggregated sites have an enhanced, presumably nonradiative, relaxation pathway to the ground state, and finally, (v) the power dependence of the TA signal indicates that there is exciton migration within the aggregated sites, despite predictions that would imply that H-aggregates would constitute traps with greatly compromised excited-state mobility.

**Discussion in Context of OPVs.** To further demonstrate the context and value of the TA data, we repeat here how EnT is vital for an OPV device. Homoenergy transfer from monomer to monomer will allow a photogenerated excited state to move quickly from the location of absorbance to the heterojunction interface.<sup>11,53</sup> A large volume may thus be sampled before the heterojunction is encountered, where ultrafast charge transfer will take place. EnT from a monomer to an aggregate may also play a role in which a downhill energy cascade<sup>54</sup> can be followed as the monomer's energy is transferred into the lower energy states of this aggregate. However, it might be expected that the low energy state of an H-aggregate will act as a trap because of its largely diminished fluorescence and therefore aggregate-to-aggregate homoenergy transfer is greatly compromised. Nevertheless, there will also be a distribution of coupling within the aggregate population<sup>22</sup> and therefore, although the lowest energy state may not fluoresce, there may be thermally accessible bright states that lie within 2 V (eq 4) of the dark state that can facilitate EnT. One would therefore expect all excitation to be funneled into the dark low-energy-aggregated sites, and as the overall order increases in the SQ sample, increasing *V*, the excitations would become more and more trapped to the low energy sites, which can be quenched by nonradiative coupling to the ground state. Therefore, when the packing order is further induced through annealing in a solar cell, the exciton's diffusion length will likely decrease. It may be advantageous to incorporate closely packed chromophores with disordered orientations so that they preserve some radiative coupling to the ground state that can facilitate EnT and exciton mobility.

One goal of our work is to consider how device efficiency can be improved through a deeper mechanistic understanding that can lead to rational design of better materials and device architectures. This work therefore leads us to consider the relative importance of (i) homo-EnT between monomers, (ii) EnT from monomers to aggregates, and (iii) EnT through a distribution of aggregates; all are important because efficient exciton diffusion is a requirement for a higher efficiency device. Our data build a picture in these systems in which rapid EnT among similar populations of chromophores, "homotransfer", leads to rapid migration of excitons in <3 ps when the concentration of dyes is >1%. By the time 3–10 homotransfer events have occurred, based on the time scales in Tables 1 and 2, the monomer-like population has been quenched by EnT to more aggregated chromophores which, due to the strong Coulombic coupling between nearby transition dipoles, have lower energy electronic states that act as sinks for nearby excitons. Finally, on a longer time scale of hundreds of picoseconds, the excitons in the aggregated species migrate through the aggregated population being eventually quenched by nonradiative processes.

Of particular interest, our interpretation of the blue-shifted bleaching recovery presented here is wholly consistent with the heavy dominance of H-aggregates upon tight packing of SQs, described in more detail by Zheng et al.<sup>52</sup> However, despite the forbidden nature of FRET-based exciton migration in H-aggregates, we measure significant exciton annihilation in the aggregates and we unexpectedly raise the vital question as to how aggregate–aggregate EnT takes place.<sup>53</sup> It is likely that the random orientation of chromophores in these solid solutions, as opposed to annealed crystalline states, preserves oscillator strength in thermally accessible states that would have been completely eliminated in an ideal  $\pi$ -stacked aggregate. We

expect that this is an important benefit of poorly packed chromophore arrays: they preserve optical activity of both the low- and high-energy states produced by Coulombic coupling, thereby enhancing opportunities for EnT and exciton migration to occur.

Nevertheless, with a randomized distribution of quadrupolar SQs (monomers and a variety of Coulombically bound aggregates), we recognize that an energy cascade exists, which will provide a directionality of the EnT, likely toward low-energy dark states of strongly coupled H-aggregates. We have often questioned why annealing our samples in devices leads to lower efficiencies even when the domain size remains fixed,<sup>20</sup> but we consider our interpretations here to mean that upon forming a more crystalline morphology, we reduce the population of weakly coupled aggregates in favor of the strongly coupled aggregates and their associated dark states which lead to *much lower exciton diffusion lengths*.

## CONCLUSIONS

In conclusion, we have investigated the excited-state properties of isolated and Coulombically coupled SQs in solid solutions, where aggregation is random, analogous to the structure that may be typical in the optimized as-cast SQ–fullerene OPV devices.<sup>23</sup> We have interpreted exciton–exciton annihilation in terms of EnT and exciton diffusion of these excited states as a function of ever decreasing intermolecular separation distance. The presence of an energy cascade driven by morphology has additional value because it challenges the notion that in molecular systems, there is little dispersion and that the landscape is homogeneous.<sup>53</sup> We can understand how the efficiency of OPV devices can be improved as we now better understand a tradeoff between efficient EnT and the formation of trap states. Low concentration monomers give rise to lower rates of EnT but there are no trap states for such monomers. On the other hand, aggregates are populated very efficiently when dyes are in high concentration and the energy is funneled into dark trap states; these states may not be expected to participate in high-speed EnT. Such aggregates are likely to form in many closely interacting push–pull molecular and polymeric OPV active layer materials. As a result, we propose a need to maintain a broad distribution of Coulombic coupling strengths in these molecular active layers in order to facilitate EnT and exciton diffusion in BHJ OPV devices. Nevertheless, devices continue to work despite the significant population of H-aggregate dark states, and more work to measure the EnT in neat SQ films is ongoing.

## ASSOCIATED CONTENT

### Supporting Information

The Supporting Information is available free of charge at <https://pubs.acs.org/doi/10.1021/acs.jpcc.9b11816>.

TA decay spectra; time-correlated single photon counting data; time constants and amplitudes for decays; steady-state PMMA UV–vis data; and spectral simulations (PDF)

## AUTHOR INFORMATION

### Corresponding Author

Christopher J. Collison – School of Chemistry and Materials Science, Nanopower Research Laboratories, and Microsystems Engineering, Rochester Institute of Technology, Rochester, New

York 14623, United States; [orcid.org/0000-0003-1301-3401](https://orcid.org/0000-0003-1301-3401); Email: [cjscha@rit.edu](mailto:cjscha@rit.edu)

## Authors

**Chenyu Zheng** – Nanopower Research Laboratories and Microsystems Engineering, Rochester Institute of Technology, Rochester, New York 14623, United States

**Michael F. Mark** – Department of Chemistry, University of Rochester, Rochester, New York 14627, United States

**Tyler Wiegand** – Nanopower Research Laboratories and Microsystems Engineering, Rochester Institute of Technology, Rochester, New York 14623, United States

**Steven A. Diaz** – Department of Chemistry, University of Rochester, Rochester, New York 14627, United States

**Jeremy Cody** – School of Chemistry and Materials Science, Rochester Institute of Technology, Rochester, New York 14623, United States

**Frank C. Spano** – Department of Chemistry, Temple University, Philadelphia, Pennsylvania 19122, United States; [orcid.org/0000-0003-3044-6727](https://orcid.org/0000-0003-3044-6727)

**David W. McCamant** – Department of Chemistry, University of Rochester, Rochester, New York 14627, United States

Complete contact information is available at:  
<https://pubs.acs.org/10.1021/acs.jpcc.9b11816>

## Author Contributions

The manuscript was written through contributions of all authors. All authors have given approval to the final version of the manuscript.

## Funding

This work was supported by the U.S. National Science Foundation (NSF) via grant numbers CBET-1603372, CHE-1566080, CHE-1900125, SusChEM-1603461.

## Notes

The authors declare no competing financial interest.

## ACKNOWLEDGMENTS

This work was carried out with the financial support for C.Z. and C.J.C. from the National Science Foundation (CBET-1603372) and for T.W. from RIT's Microsystems Engineering PhD program. M.F.M., S.A.D., and D.W.M. were supported by the U.S. National Science Foundation (NSF) via grant numbers CHE-1566080 and CHE-1900125. F.C.S. has financial support from the National Science Foundation (SusChEM-1603461).

## REFERENCES

- (1) Lin, Y.; Dam, H. F.; Andersen, T. R.; Bundgaard, E.; Fu, W.; Chen, H.; Krebs, F. C.; Zhan, X. Ambient Roll-to-Roll Fabrication of Flexible Solar Cells Based on Small Molecules. *J. Mater. Chem. C* **2013**, *1*, 8007–8010.
- (2) Carlé, J. E.; Krebs, F. C. Technological Status of Organic Photovoltaics (OPV). *Sol. Energy Mater. Sol. Cells* **2013**, *119*, 309–310.
- (3) Darling, S. B.; You, F. The Case for Organic Photovoltaics. *RSC Adv.* **2013**, *3*, 17633–17648.
- (4) Zhao, W.; Li, S.; Yao, H.; Zhang, S.; Zhang, Y.; Yang, B.; Hou, J. Molecular Optimization Enables over 13% Efficiency in Organic Solar Cells. *J. Am. Chem. Soc.* **2017**, *139*, 7148–7151.
- (5) Sun, J.; Ma, X.; Zhang, Z.; Yu, J.; Zhou, J.; Yin, X.; Yang, L.; Geng, R.; Zhu, R.; Zhang, F.; et al. Dithieno[3,2-b:2',3'-d]Pyrrole Fused Nonfullerene Acceptors Enabling Over 13% Efficiency for Organic Solar Cells. *Adv. Mater.* **2018**, *30*, 1707150.

- (6) Li, W.; Ye, L.; Li, S.; Yao, H.; Ade, H.; Hou, J. A High-Efficiency Organic Solar Cell Enabled by the Strong Intramolecular Electron Push–Pull Effect of the Nonfullerene Acceptor. *Adv. Mater.* **2018**, *30*, 1707170.
- (7) Zuo, L.; Shi, X.; Jo, S. B.; Liu, Y.; Lin, F.; Jen, A. K.-Y. Tackling Energy Loss for High-Efficiency Organic Solar Cells with Integrated Multiple Strategies. *Adv. Mater.* **2018**, *30*, 1706816.
- (8) Che, X.; Li, Y.; Qu, Y.; Forrest, S. R. High Fabrication Yield Organic Tandem Photovoltaics Combining Vacuum- and Solution-Processed Subcells with 15% Efficiency. *Nat. Energy* **2018**, *3*, 422.
- (9) Meng, L.; Zhang, Y.; Wan, X.; Li, C.; Zhang, X.; Wang, Y.; Ke, X.; Xiao, Z.; Ding, L.; Xia, R.; et al. Organic and Solution-Processed Tandem Solar Cells with 17.3% Efficiency. *Science* **2018**, *361*, 1094–1098.
- (10) Ostroverkhova, O. Organic Optoelectronic Materials: Mechanisms and Applications. *Chem. Rev.* **2016**, *116*, 13279–13412.
- (11) Hedley, G. J.; Ruseckas, A.; Samuel, I. D. W. Light Harvesting for Organic Photovoltaics. *Chem. Rev.* **2017**, *117*, 796–837.
- (12) Pelzer, K. M.; Darling, S. B. Charge Generation in Organic Photovoltaics: A Review of Theory and Computation. *Mol. Syst. Des. Eng.* **2016**, *1*, 10–24.
- (13) Speller, E. M.; Clarke, A. J.; Luke, J.; Lee, H. K. H.; Durrant, J. R.; Li, N.; Wang, T.; Wong, H. C.; Kim, J.-S.; Tsoi, W. C.; et al. From Fullerene Acceptors to Non-Fullerene Acceptors: Prospects and Challenges in the Stability of Organic Solar Cells. *J. Mater. Chem. A* **2019**, *7*, 23361.
- (14) Hestand, N. J.; Spano, F. C. Molecular Aggregate Photophysics beyond the Kasha Model: Novel Design Principles for Organic Materials. *Acc. Chem. Res.* **2017**, *50*, 341–350.
- (15) Tamai, Y.; Ohkita, H.; Bente, H.; Ito, S. Exciton Diffusion in Conjugated Polymers: From Fundamental Understanding to Improvement in Photovoltaic Conversion Efficiency. *J. Phys. Chem. Lett.* **2015**, *6*, 3417–3428.
- (16) Spano, F. C. Modeling Disorder in Polymer Aggregates: The Optical Spectroscopy of Regioregular Poly(3-Hexylthiophene) Thin Films. *J. Chem. Phys.* **2005**, *122*, 234701.
- (17) Spano, F. C. The Spectral Signatures of Frenkel Polarons in H- and J-Aggregates. *Acc. Chem. Res.* **2010**, *43*, 429–439.
- (18) Hestand, N. J.; Spano, F. C. Expanded Theory of H- and J-Molecular Aggregates: The Effects of Vibronic Coupling and Intermolecular Charge Transfer. *Chem. Rev.* **2018**, *118*, 7069.
- (19) Turro, N. J.; Scaiano, J. C.; Ramamurthy, V. *Modern Molecular Photochemistry of Organic Molecules*, 1st ed.; University Science Books: Sausalito, Calif, 2010.
- (20) Hestand, N. J.; Zheng, C.; Penmetcha, A. R.; Cona, B.; Cody, J. A.; Spano, F. C.; Collison, C. J. Confirmation of the Origins of Panchromatic Spectra in Squaraine Thin Films Targeted for Organic Photovoltaic Devices. *J. Phys. Chem. C* **2015**, *119*, 18964–18974.
- (21) Zheng, C.; Bleier, D.; Jalan, I.; Pristash, S.; Penmetcha, A. R.; Hestand, N. J.; Spano, F. C.; Pierce, M. S.; Cody, J. A.; Collison, C. J. Phase Separation, Crystallinity and Monomer-Aggregate Population Control in Solution Processed Small Molecule Solar Cells. *Sol. Energy Mater. Sol. Cells* **2016**, *157*, 366–376.
- (22) Zheng, C.; Zhong, C.; Collison, C. J.; Spano, F. C. Non-Kasha Behavior in Quadrupolar Dye Aggregates: The Red-Shifted H-Aggregate. *J. Phys. Chem. C* **2019**, *123*, 3203–3215.
- (23) Zheng, C.; Penmetcha, A. R.; Cona, B.; Spencer, S. D.; Zhu, B.; Heaphy, P.; Cody, J. A.; Collison, C. J. Contribution of Aggregate States and Energetic Disorder to a Squaraine System Targeted for Organic Photovoltaic Devices. *Langmuir* **2015**, *31*, 7717–7726.
- (24) Zheng, C.; Jalan, I.; Cost, P.; Oliver, K.; Gupta, A.; Mixture, S.; Cody, J. A.; Collison, C. J. Impact of Alkyl Chain Length on Small Molecule Crystallization and Nanomorphology in Squaraine-Based Solution Processed Solar Cells. *J. Phys. Chem. C* **2017**, *121*, 7750–7760.
- (25) Spencer, S.; Cody, J.; Mixture, S.; Cona, B.; Heaphy, P.; Rumbles, G.; Andersen, J.; Collison, C. Critical Electron Transfer Rates for Exciton Dissociation Governed by Extent of Crystallinity in



Small Molecule Organic Photovoltaics. *J. Phys. Chem. C* **2014**, *118*, 14840–14847.

(26) Chen, G.; Sasabe, H.; Igarashi, T.; Hong, Z.; Kido, J. Squaraine Dyes for Organic Photovoltaic Cells. *J. Mater. Chem. A* **2015**, *3*, 14517–14534.

(27) Yang, D.; Yang, Q.; Yang, L.; Luo, Q.; Huang, Y.; Lu, Z.; Zhao, S. Novel High Performance Asymmetrical Squaraines for Small Molecule Organic Solar Cells with a High Open Circuit Voltage of 1.12 V. *Chem. Commun.* **2013**, *49*, 10465–10467.

(28) Spencer, S.; Hu, H.; Li, Q.; Ahn, H.-Y.; Qaddoura, M.; Yao, S.; Ioannidis, A.; Belfield, K.; Collison, C. J. Controlling J-Aggregate Formation for Increased Short-Circuit Current and Power Conversion Efficiency with a Squaraine Donor. *Prog. Photovolt. Res. Appl.* **2014**, *22*, 488–493.

(29) Wei, G.; Xiao, X.; Wang, S.; Zimmerman, J. D.; Sun, K.; Diev, V. V.; Thompson, M. E.; Forrest, S. R. Arylamine-Based Squaraine Donors for Use in Organic Solar Cells. *Nano Lett.* **2011**, *11*, 4261–4264.

(30) Chen, G.; Sasabe, H.; Wang, Z.; Wang, X.; Hong, Z.; Kido, J.; Yang, Y. Solution-Processed Organic Photovoltaic Cells Based on a Squaraine Dye. *Phys. Chem. Chem. Phys.* **2012**, *14*, 14661–14666.

(31) Mayerhöffer, U.; Deing, K.; Gruß, K.; Braunschweig, H.; Meerholz, K.; Würthner, F. Outstanding Short-Circuit Currents in BHJ Solar Cells Based on NIR-Absorbing Acceptor-Substituted Squaraines. *Angew. Chem., Int. Ed.* **2009**, *48*, 8776–8779.

(32) Yang, D.; Sasabe, H.; Jiao, Y.; Zhuang, T.; Huang, Y.; Pu, X.; Sano, T.; Lu, Z.; Kido, J. An Effective  $\pi$ -Extended Squaraine for Solution-Processed Organic Solar Cells with High Efficiency. *J. Mater. Chem. A* **2016**, *4*, 18931–18941.

(33) Goh, T.; Huang, J.-S.; Yager, K. G.; Sfeir, M. Y.; Nam, C.-Y.; Tong, X.; Guard, L. M.; Melvin, P. R.; Antonio, F.; Bartolome, B. G.; et al. Quaternary Organic Solar Cells Enhanced by CocrySTALLINE Squaraines with Power Conversion Efficiencies >10%. *Adv. Energy Mater.* **2016**, *6*, 1600660.

(34) Jemison, R. C.; McCullough, R. D. Techniques for the Molecular Design of Push-Pull Polymers towards Enhanced Organic Photovoltaic Performance. *Polymer Composites for Energy Harvesting, Conversion, and Storage*; ACS Symposium Series; American Chemical Society, 2014; Vol. 1161, pp 71–109.

(35) Coffey, T.; Seredinski, A.; Poler, J. N.; Patteson, C.; Watts, W. H.; Baptiste, K.; Zheng, C.; Cody, J.; Collison, C. J. Nanoscale Characterization of Squaraine-Fullerene-Based Photovoltaic Active Layers by Atomic Force Microscopy Mechanical and Electrical Property Mapping. *Thin Solid Films* **2019**, *669*, 120.

(36) Wei, G.; Wang, S.; Sun, K.; Thompson, M. E.; Forrest, S. R. Solvent-Annealed Crystalline Squaraine: PC70BM (1:6) Solar Cells. *Adv. Energy Mater.* **2011**, *1*, 184–187.

(37) Wei, G.; Lunt, R. R.; Sun, K.; Wang, S.; Thompson, M. E.; Forrest, S. R. Efficient, Ordered Bulk Heterojunction Nanocrystalline Solar Cells by Annealing of Ultrathin Squaraine Thin Films. *Nano Lett.* **2010**, *10*, 3555–3559.

(38) Penzkofer, A.; Lu, Y. Fluorescence Quenching of Rhodamine 6G in Methanol at High Concentration. *Chem. Phys.* **1986**, *103*, 399–405.

(39) Gardner, K.; Aghajamali, M.; Vagin, S.; Pille, J.; Morrish, W.; Veinot, J. G. C.; Rieger, B.; Meldrum, A. Ultrabright Fluorescent and Lasing Microspheres from a Conjugated Polymer. *Adv. Funct. Mater.* **2018**, *28*, 1802759.

(40) Dirk, C. W.; Herndon, W. C.; Cervantes-Lee, F.; Selnau, H.; Martinez, S.; Kalamegham, P.; Tan, A.; Campos, G.; Velez, M. Squarylium Dyes: Structural Factors Pertaining to the Negative Third-Order Nonlinear Optical Response. *J. Am. Chem. Soc.* **1995**, *117*, 2214–2225.

(41) Cerullo, G.; Nisoli, M.; Stagira, S.; De Silvestri, S. Sub-8-Fs Pulses from an Ultrabroadband Optical Parametric Amplifier in the Visible. *Opt. Lett.* **1998**, *23*, 1283–1285.

(42) Cerullo, G.; De Silvestri, S. Ultrafast Optical Parametric Amplifiers. *Rev. Sci. Instrum.* **2003**, *74*, 1–18.

(43) Trebino, R.; DeLong, K. W.; Fittinghoff, D. N.; Sweetser, J. N.; Krumbügel, M. A.; Richman, B. A.; Kane, D. J. Measuring Ultrashort Laser Pulses in the Time-Frequency Domain Using Frequency-Resolved Optical Gating. *Rev. Sci. Instrum.* **1997**, *68*, 3277–3295.

(44) Kasha, M.; Rawls, H. R.; Ashraf El-Bayoumi, M. The Exciton Model in Molecular Spectroscopy. *Pure Appl. Chem.* **1965**, *11*, 371–392.

(45) Law, K.-Y. Squaraine Chemistry: Effects of Solvent and Temperature on the Fluorescence Emission of Squaraines. *J. Photochem. Photobiol., A* **1994**, *84*, 123–132.

(46) Liu, T.; Bondar, M. V.; Belfield, K. D.; Anderson, D.; Masunov, A. E.; Hagan, D. J.; Stryland, E. W. V. Linear Photophysics and Femtosecond Nonlinear Spectroscopy of a Star-Shaped Squaraine Derivative with Efficient Two-Photon Absorption. *J. Phys. Chem. C* **2016**, *120*, 11099–11110.

(47) Lakowicz, J. R. *Principles of Fluorescence Spectroscopy*, 3rd ed.; Springer US, 2006.

(48) Lessing, H. E.; Von Jena, A. Separation of Rotational Diffusion and Level Kinetics in Transient Absorption Spectroscopy. *Chem. Phys. Lett.* **1976**, *42*, 213–217.

(49) Min, C.-K.; Joo, T.; Yoon, M.-C.; Kim, C. M.; Hwang, Y. N.; Kim, D.; Aratani, N.; Yoshida, N.; Osuka, A. Transient Absorption Anisotropy Study of Ultrafast Energy Transfer in Porphyrin Monomer, Its Direct Meso–Meso Coupled Dimer and Trimer. *J. Chem. Phys.* **2001**, *114*, 6750–6758.

(50) Baumann, J.; Fayer, M. D. Excitation Transfer in Disordered Two-dimensional and Anisotropic Three-dimensional Systems: Effects of Spatial Geometry on Time-resolved Observables. *J. Chem. Phys.* **1986**, *85*, 4087–4107.

(51) Krider, E. P. Spatial Distribution of Lightning Strikes to Ground during Small Thunderstorms in Florida. *International Aerospace and Ground Conference on Lightning and Static Electricity*, 1988.

(52) Krider, E. P. On the Chances of Being Struck by Cloud-to-Ground Lightning. In *2003 IEEE Bologna Power Tech Conference Proceedings*, 2003; Vol. 3, p 4.

(53) Menke, S. M.; Holmes, R. J. Exciton Diffusion in Organic Photovoltaic Cells. *Energy Environ. Sci.* **2014**, *7*, 499–512.

(54) Reid, O. G.; Rumbles, G. Resonance Energy Transfer Enables Efficient Planar Heterojunction Organic Solar Cells. *J. Phys. Chem. C* **2016**, *120*, 87–97.

(55) Terenziani, F.; Painelli, A.; Katan, C.; Charlot, M.; Blanchard-Desce, M. Charge Instability in Quadrupolar Chromophores: Symmetry Breaking and Solvatochromism. *J. Am. Chem. Soc.* **2006**, *128*, 15742–15755.

(56) Shafeekh, K. M.; Das, S.; Sissa, C.; Painelli, A. Asymmetric Squaraine Dyes: Spectroscopic and Theoretical Investigation. *J. Phys. Chem. B* **2013**, *117*, 8536–8546.